Aerosol assisted CVD grown WO_3 nanoneedles decorated with Cu_2O nanoparticles for the selective and humidity resilient detection of H_2S

Fatima E. Annanouch,[†] Zouhair Haddi,[†] Stella Vallejos,[‡,^] Polona Umek,[§] Peter Guttmann,[#] Carla Bittencourt,[ɣ] and Eduard Llobet[*,†]*

[†]Research Centre on the Engineering of Materials and micro/nano Systems (EMaS), Universitat Rovira i Virgili Països Catalans 26, 43007 Tarragona, Spain, [‡]SIX Research Center, Faculty of Electrical Engineering and Communication, Brno University of Technology, Technicka 12, CZ-61600 Brno, Czech Republic, [^]Instituto de Microelectrónica de Barcelona, Consejo Superior de Investigaciones Científicas, Campus UAB, 08193 Bellaterra, Barcelona, Spain, [§]Solid State, Physics Department, Jožef Stefan Institute, 39 Jamova cesta, 1000 Ljubljana, Slovenia, [#]Helmholtz-Zentrum Berlin für Materialien und Energie GmbH, Institute for Soft Matter and Functional Materials, Albert-Einstein-Str. 15, 12489 Berlin, Germany, [ɣ]Plasma-Surface Interaction Chemistry (ChiPS) University of Mons 1 Copernic, 7000 Mons, Belgium

KEYWORDS: aerosol assisted CVD, nanoneedles, nanoparticles, functionalization, gas sensor

[*] Address correspondence to eduard.llobet@urv.cat

ABSTRACT

A gas-sensitive hybrid material consisting of Cu_2O nanoparticle-decorated WO_3 nanoneedles is successfully grown for the first time in a single step via aerosol assisted chemical vapor deposition. The morphological, structural, and composition analysis show that our method is effective for growing single crystalline, *n*-type WO_3 nanoneedles decorated with *p*-type Cu_2O nanoparticles at moderate temperatures (i.e., 380 °C), with cost effectiveness and short fabrication times, directly onto micro-hotplate transducer arrays in view of obtaining gas sensors. The gas sensing studies performed show that this hybrid nanomaterial has excellent sensitivity and selectivity to hydrogen sulfide (7-fold increase in response compared with that of pristine WO_3 nanoneedles), a low detection limit (below 300 ppb of H_2S) together with unprecedented fast response times (2 s) and high immunity to changes in background humidity. These superior properties arise due to the multiple *p*-*n* heterojunctions created at the nanoscale in our hybrid nanomaterial.

Introduction

Hydrogen sulfide (H_2S) is a colorless, flammable and very poisoning gas with a characteristic smell of rotten eggs. It can be released from sewage, manure, hot springs and food processing.[1] The acceptable ambient limit for H_2S (recommended by the Scientific Advisory Board on Toxic Air Pollutants, USA) is in the range of 20–100 ppb,[2] while the typical permissible exposure limit of this gas according to the US Occupational Safety and Health Administration is about 10 ppm.[3,4] People exposed to a concentration above this value can experience irritation of the eyes, nose, and respiratory system, while higher concentrations (250 ppm) can cause death.[3,5] Nowadays, commercially-available H_2S detectors rely either on electrochemical or solid-state

metal oxide sensors. While the former are difficult to miniaturize and rather expensive, the latter suffer from poor selectivity and heavy humidity cross-sensitivity. Additionally, both types of sensors allow for reliably estimating H_2S concentrations in the tens of ppm range with uncertainties near ±5 ppm. Therefore, there is a need and a strong industry-driven demand for developing a new generation of reliable, robust, accurate and cost effective sensors with enhanced sensitivity and selectivity, reduced moisture cross-sensitivity and response time to facilitate the early detection of hydrogen sulfide in the environment, before its concentration reaches potentially hazardous levels.

In the last few years, *n*-type metal oxide semiconductors (i.e., SnO_2, In_2O_3, ZnO or WO_3) with different morphologies such as nanoparticle films or one-dimensional nanostructures, have been intensively explored as potential building-blocks for H_2S gas sensors.[6,7] The research on one-dimensional (1-D), single crystalline metal oxide nanostructures including nanowires, nanotubes, nanoneedles, nanorods and nanobelts, has been favored in the recent years, since their ultrahigh surface-to-volume ratio, low number of defects and good stability within a wide range of operating temperatures, make them an excellent building-block for micro/nanoscale gas sensors.[8-10] Yet, the lack of selectivity together with humidity cross-sensitivity still remain the major drawbacks to be overcome. Many works have shown that by adding catalyst nanoparticles onto the metal oxide matrix (i.e., surface functionalization of the low-dimensional metal oxide), the selectivity toward a target gas can be significantly increased.[10-14] In general, the growth of functionalized, nanostructured materials employs a multi-step approach in which in the first step the nanostructured materials are synthesized. This is followed in the second step by a functionalization in which metal nanoparticles are deposited onto the surface of the previously grown nanostructures. In some cases, the process still needs a third step in which the as-

deposited metal nanoparticles are oxidized. This involved, multi-step process can not be easily scaled up and, therefore, will hardly be adopted by the industry for mass production of sensors.[15] The use of *n*-type metal oxide nanomaterials functionalized with *p*-type, cupric oxide nanoparticles has been reported to be advantageous for detecting hydrogen sulfide. Shao and co-workers reported with CuO nanoparticle decorated SnO_2 nanowires for detecting H_2S with high sensitivity and remarkable selectivity.[16] Yet, the response time of their sensor was rather long (i.e., 3 minutes) and response was significantly reduced for hydrogen sulfide concentrations below 1 ppm. Furthermore, the sensing material was produced following a time consuming three-step technique that included two conventional CVD processes followed by a 24 h oxidation (for growing the metal oxide nanowires, decorating them with Cu nanoparticles and oxidizing the latter to CuO). Sun and co-workers also addressed the detection of H_2S using CuO-SnO_2 nanowires.[17] Although their sensor was not as responsive as the one presented by Shao and co-workers, the response time was clearly improved down to 9 seconds. However, the synthesis process remained complex and lengthy. Wu and co-workers studied ZnO nanorods for the detection of H_2S at room temperature.[18] Although a remarkable response was obtained for 1 ppm of hydrogen sulfide, a rather long response time of about 20 minutes was observed and the sensor was unable to recover its original baseline after the exposure to the analyte. Finally, none of the papers cited above reported the effect of ambient humidity on sensor response, yet it is well known that humidity cross-sensitivity is a major problem experienced with metal oxide gas sensors.

Recently, we have shown that aerosol assisted chemical vapor deposition (AACVD), is a suitable method for growing, in a single step, tungsten oxide nanoneedles decorated with metal nanoparticles.[9,13,19] Unlike in conventional CVD, where precursors must be volatile and

thermally stable, AACVD allows for the use of a wide range of precursors owing to its solution-delivery based principle.[6] Furthermore, the AACVD process is conducted at lower temperatures than CVD, typically in a range between 350 and 600 ºC, which makes it suitable for the direct, bottom-up integration of gas-sensitive nanomaterials onto a wide spectrum of substrates including glass, ceramic, silicon micro electro-mechanical systems (MEMS) or even flexible polymeric.[20] In this paper we report, for the first time, on the direct growth of tungsten trioxide (WO_3) nanoneedles decorated with *p*-type Cu_2O nanoparticles onto MEMS hotplates in a single step, by using AACVD. To the best of our knowledge, CVD routes have not been used before to grow WO_3 nanoneedles and simultaneously decorate then with nanoparticles of copper oxides, all in a single step and avoiding a further oxidation step. Scanning electron microscopy (SEM), X-ray diffraction (XRD), transmission electron microscopy (TEM), high resolution TEM (HRTEM), X-ray photoelectron spectroscopy (XPS) and near edge X-ray absorption fine structure transmission X-ray microscope (NEXAFS-TXM), have been employed to determine phase composition, morphology and microstructure of the as nanoneedle mats. Their gas sensing properties toward H_2S both in dry and humid backgrounds have been studied, together with their response to other gases or vapors. Finally, in light of the experimental findings, a sensing mechanism for hydrogen sulfide in Cu_2O-decorated tungsten oxide nanoneedles is introduced and discussed.

Results and discussion

Materials characterization

Pure WO_3 nanoneedles were obtained from the AACVD of $W(CO)_6$ at 500 °C. WO_3 nanoneedles decorated with Cu_2O were grown in a single step, at a lower temperature of 380 °C

from the AACVD of a mixture of $W(CO)_6$ and $Cu(acac)_2$. The as-deposited films (WO_3 and Cu_2O/WO_3) were strongly adherent to the substrate, with dark blue and dark maroon-blue color, respectively. After annealing at 500 °C for 3 h, the color of both samples changed, and became white-yellow. The morphology of the synthesized materials was characterized by scanning electron microscopy. Figure 1 depicts the SEM images obtained from the as-deposited layers. The results confirm the formation of a thicker layer of non-aligned nanoneedle-like structures, with high density and homogenous distribution over the substrate. The nanoneedles of pure tungsten oxides (Figure 1.a and c) were ~ 11 microns long and their diameter varied between 50–100 nm. Cu_2O/WO_3 nanoneedles (Figure 1.b and d), were 5 microns long with a thicker diameter that ranged between 50 and 240 nm, agglomerates of two, three or more nanoneedles are also visible. This difference in the morphology of the nanoneedles grown in functionalized and non-functionalized samples could be attributed to the growth temperature and/or the solvent used.[21]

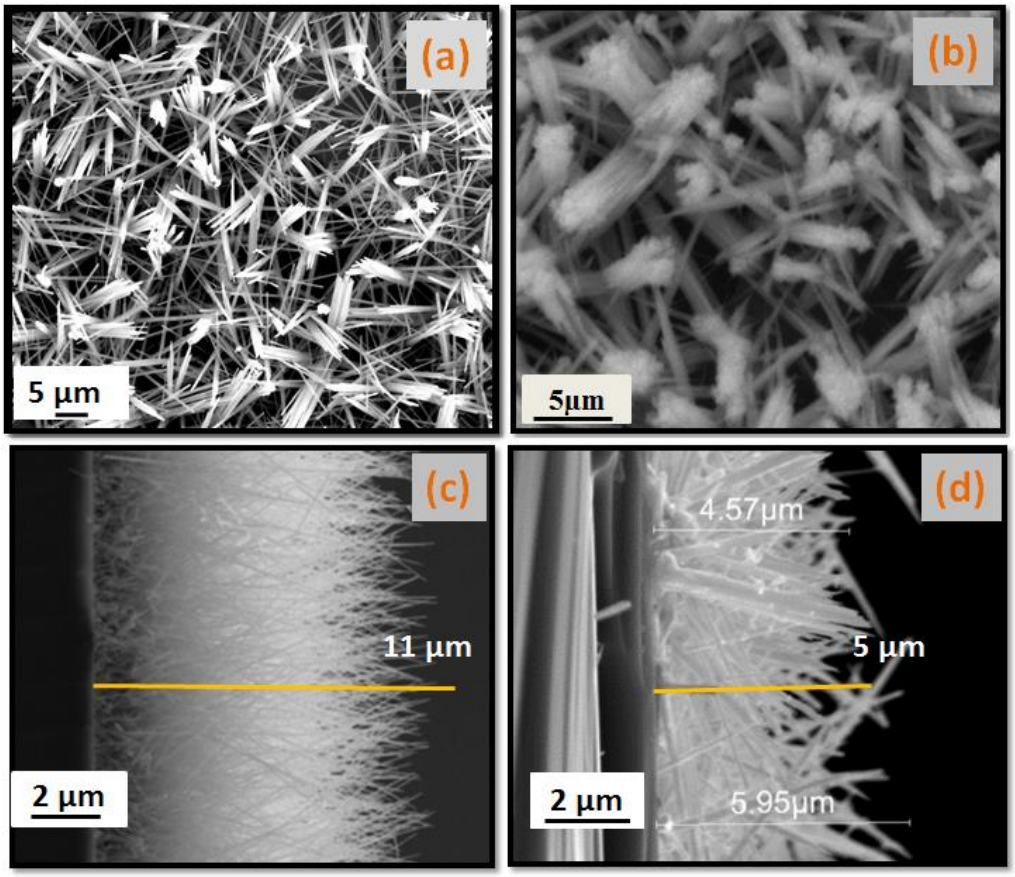

Figure 1. SEM images of the as-deposited (a) pure WO_3 nanoneedles, (b) Cu_2O functionalized WO_3 nanoneedles, (c) cross-section of pure WO_3 nanoneedles, and (d) cross-section of Cu_2O functionalized WO_3 nanoneedles.

X-ray diffraction (XRD) analysis (Figure 2) of the different samples indicated the formation of monoclinic-phase WO_3 nanoneedles (P21/n (14) space group, with typical cell parameters of a= 0.729 nm, b=0.7539 nm, c=0.7688 nm, and β=90.91º; ICCD card no. 72-0677). From the pure WO_3 pattern, it is clear that the nanoneedles were strongly oriented in the (002) direction, showing an intense diffraction peak at 23.10° 2θ. Furthermore, a strong platinum reflection at 39.9° 2θ was observed, which was coming from the electrodes. For the pattern recorded from the functionalized sample, the nanoneedles were randomly oriented, with the absence of any reflections from copper oxides.

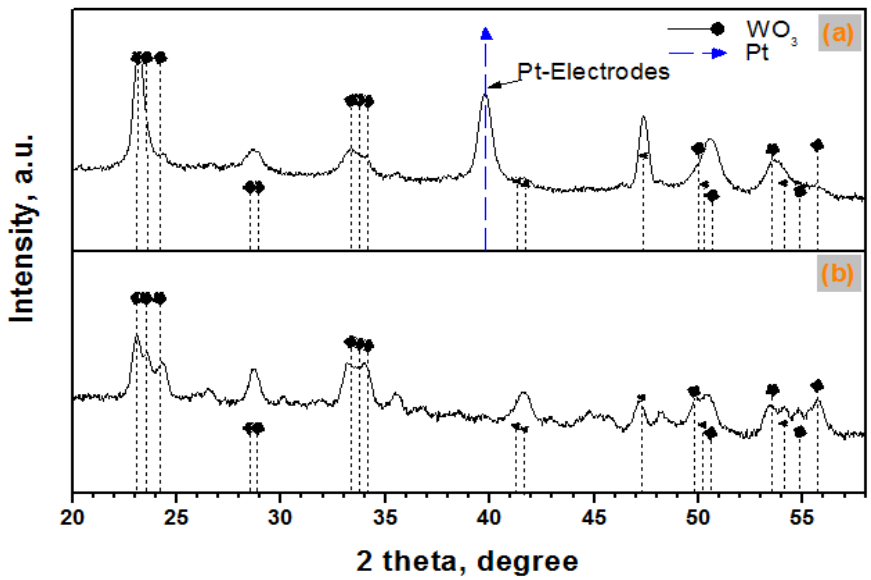

Figure 2. XRD patterns of (a) pure WO_3 nanoneedles, and (b) Cu_2O functionalized WO_3 nanoneedles.

Elemental and chemical characterizations of the films were performed by XPS. In this work, we do not show the XPS and HRTEM results obtained from pure WO_3 film, since they were similar to the ones reported in our previous works.[9,22] Figure 3.a shows the W 4f XP spectrum recorded on a Cu_2O/WO_3 sample and its fitting analysis. To reproduce the spectrum, two doublets, a singlet and the Shirley background were employed. The component centered at 38.6 eV is due to photoelectrons emitted from the W 5p3/2 core level. The highest intensity doublet peak (W $4f_{7/2}$), centered at 35.5 eV, is generated by photoelectrons emitted from W atoms with the oxidation state +6, i.e., stoichiometric WO_3.[23] Therefore, the W ions have their 5d shell empty, i.e., there are no cation d-electrons available to be transferred to adsorbates. The second W 4f doublet, found at 2 eV lower binding energy, is generated by photoelectrons emitted from W atoms with the oxidation state +4.[24] In this case, the d-electron orbitals on adjacent cations are partially occupied. These reduced cations provide active sites for chemisorption and catalytic activity, i.e., determine the gas-sensing activity of the films.[25] From the area ratio of the

components used to fit the W 4f peak we evaluated that near 35% of the tungsten atoms have the oxidation state +4, thus contributing to gas detection. This result is supported by the analysis of the O 1s XP spectrum that is reproduced by two singlets (Figure 3.b), the first component is centered at 530.5 eV and it is assigned to the oxygen atoms that form the strong W¼O bonds in the oxide.[26] The second component at about 531.7 eV (37% of the total O 1s area) has been attributed to O atoms in sub-stoichiometric WOx structures.[27]

Figure 3.c shows the Cu 2p core level spectrum, which consists of two sets of peaks: a low intensity doublet at 942.6 eV and 962.8 eV, which corresponds to CuO, and a more intense doublet which components are centered at 932.6 and 952.3 eV, which corresponds to either Cu metal or Cu_2O.

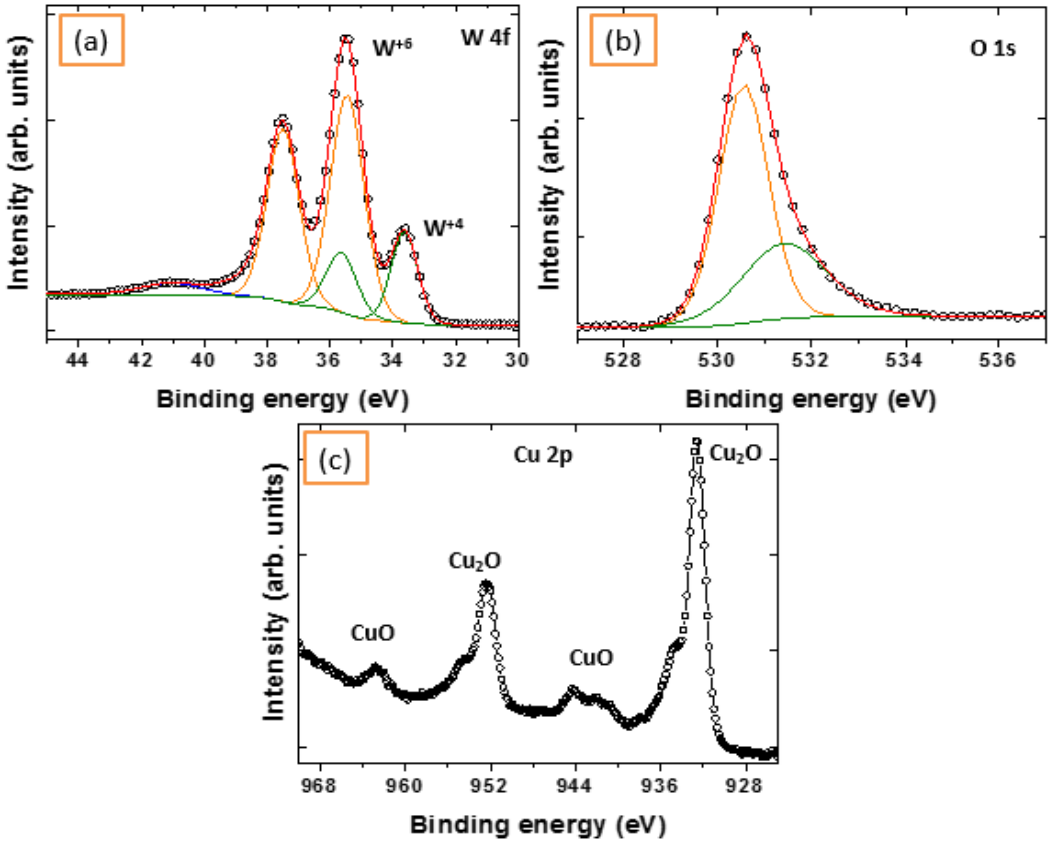

Figure 3. Typical XPS spectra of the Cu_2O nanoparticles decorated WO_3 nanoneedles (a) W 4f, (b) O 1s, and (c) Cu 2p.

In order to experimentally clarify to which oxidation state belong this doublet, we have analyzed our sample by NEXAFS-TXM. NEXAFS probing the density of states (DOS) of partially filled or completely unfilled electronic states is very sensitive to the local bonding environment, particularly to the number of valence electrons, the symmetry and coordination number of the material structural unit cell.[28] Figure 4 illustrates the copper L-edge NEXAFS spectrum, which is characterized by a low intensity feature at ~ 930.8 eV attributed to CuO and two relative intense features at ~ 932.8 and ~ 953.5 eV. These two intense features that arise from the dipole transitions of the Cu 2p3/2 and Cu 2p1/2 core levels into the empty d-states were associated to the presence of Cu_2O as reported in ref.[29] Therefore XPS and NEXAFS analysis together testify for the presence of CuO and Cu_2O in the sample, with 88% of the Cu atoms in the Cu_2O form and 12% in the CuO form.

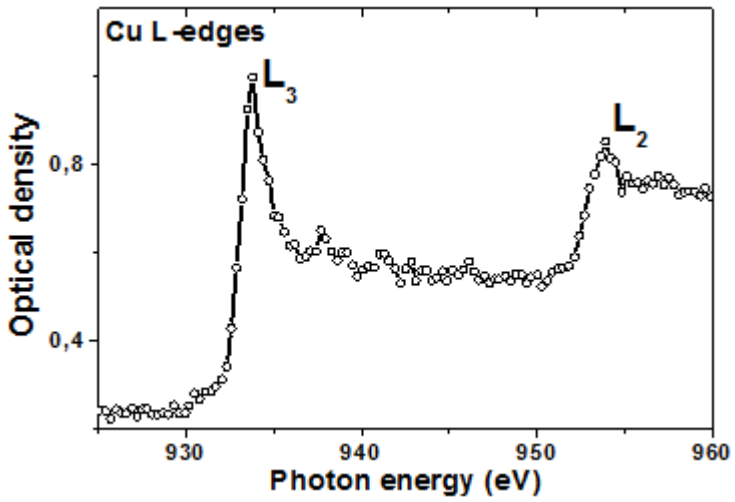

Figure 4. NEXAFS-TXM spectrum of Cu L-edges of nanoparticles decorated WO_3 nanoneedles. The energy separation between L_3 and L_2 is 21.0 eV which is characteristic for Cu_2O.

Details of morphological and structural features of Cu_2O decorated WO_3 nanoneedle mats were studied by TEM and high resolution TEM. Figure 5.a and b display the low-magnification TEM

images of Cu_2O/CuO nanoparticles decorating the nanoneedles. The formation of nanoparticles with average diameter of about 2–3 nm, and the existence of few bigger ones with diameter about 7 nm can be observed. In addition, a thin amorphous layer surrounding the nanoneedles can also be seen, the formation of which can be associated to the combustion of the solvents during the AACVD process. The analysis of high resolution TEM images (Figure 5.c and d) reveals the coexistence of Cu_2O and CuO crystallites in the Cu_2O/WO_3 nanoneedle mats.

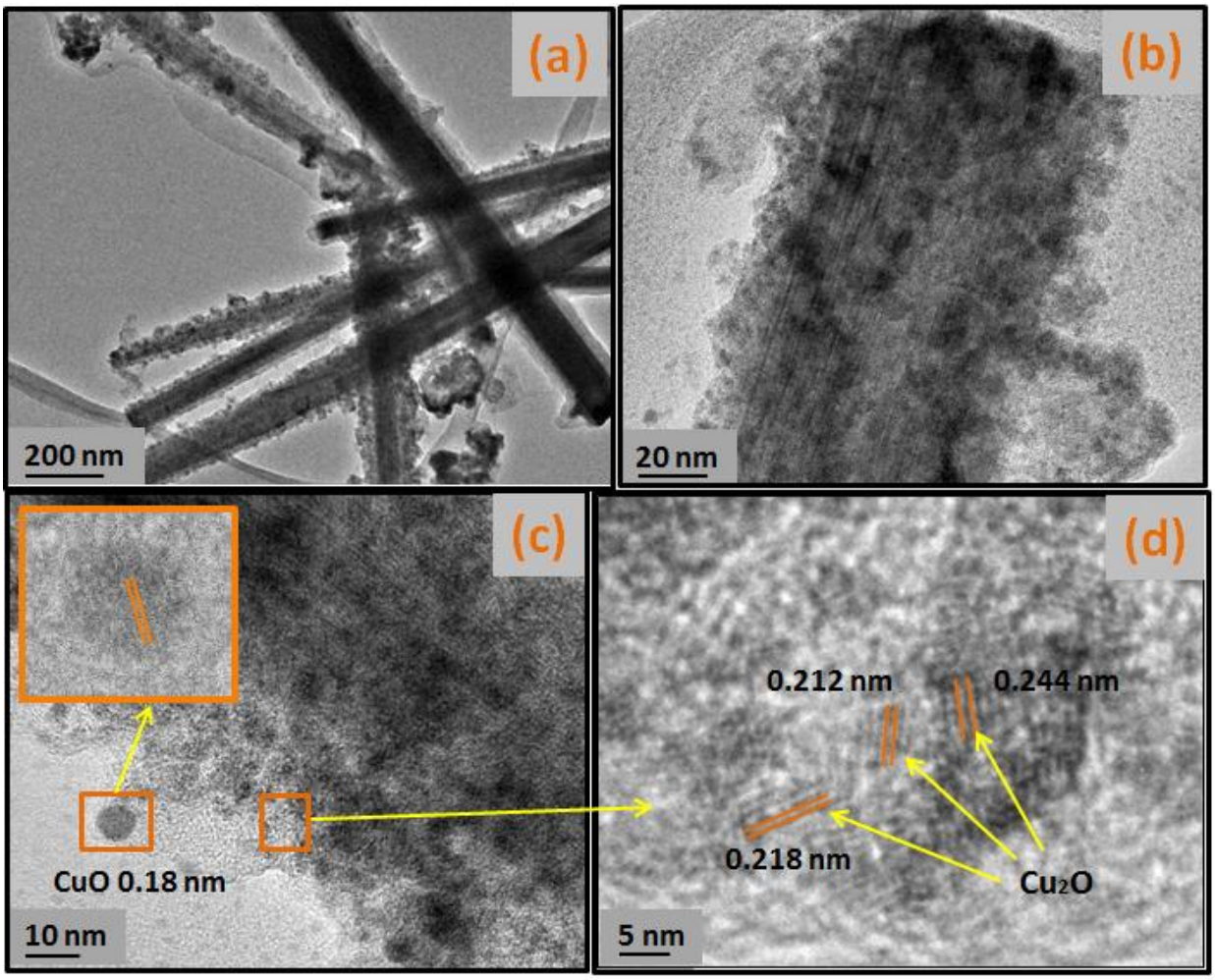

Figure 5. TEM and HRTEM images of the obtained Cu2O functionalized WO3 nanoneedles, (a&b) low magnification and (c&d) high magnification.

As derived from TEM images, the fringe patterns with the interspacing distances of 0.218, 0.244 and 0.212 nm are similar to the interplanar distances of the (200), (111) and (200) lattice planes of Cu_2O respectively (ICDD-PDF Card Nº. 00-005-0667), whereas, that with interspacing distance of 0.177 nm is in a good agreement with the interplanar distance of the (112) lattice planes in bulk crystalline CuO (ICDD-PDF Card Nº. 00-045-0937). Hence, these results suggest that the smaller nanoparticles which represent the vast majority correspond to Cu_2O and the larger ones correspond to CuO. As a summary, XPS, NEXAFS-TXM and HRTEM results imply that both CuO and Cu_2O co-exist in the samples with Cu_2O being more profuse.

Gas sensing response

The gas sensing properties toward 5 ppm of H_2S of pristine WO_3 and Cu_2O functionalized WO_3 nanoneedles were examined at operating temperatures ranging from 270 to 390 ºC. The maximum operating temperature was selected to ensure the safe operation of the sensor transducer (i.e., avoiding membrane damages or drift in the heating element). The results are shown in Figure 6.

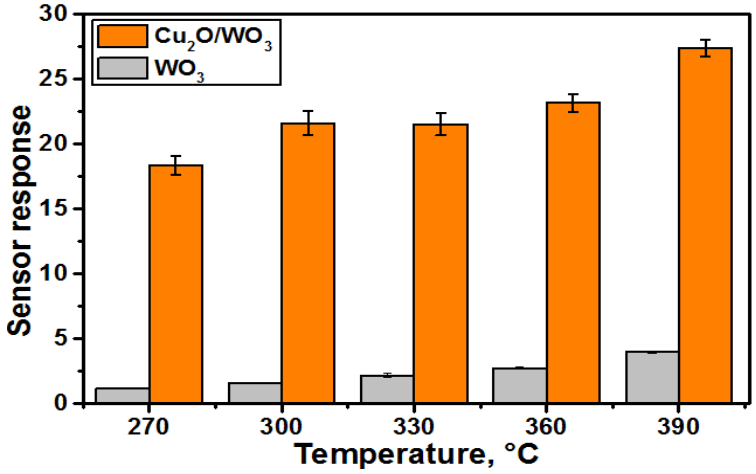

Figure 6. Sensor responses and error bars to 5 ppm of H_2S as a function of the operating temperature.

Cu_2O/WO_3 samples showed stable and very high responses all over the operating temperatures tested. In contrast, pure WO_3 nanoneedles displayed good and stable responses at temperatures equal or exceeding 280 ºC, while below this value, they exhibited unsaturated responses, with drift in the baseline resistance. For the range of temperatures tested, sensor response increases when the operating temperature is increased. Generally, in metal oxides, the optimal working temperature depends on the quantity of the adsorbed oxygen ionic species and the energy needed to enable the reactions between these ionic species and a target gas.[30,31] The highest response recorded from pristine WO_3 samples toward 5 ppm of H_2S was 4, while it reached 27.5 for Cu_2O/WO_3 nanoneedles. Thus, the decoration with Cu_2O nanoparticles of WO_3 nanoneedles has resulted in a 7-fold increase in sensor response.

In the subsequent studies, 390 °C was chosen as the optimal working temperature of the sensors. Figure 7 depicts the responses obtained from the sensors to various concentrations of H_2S, at the optimal working temperature. The insets show the curves of the response versus concentration. From these results, it is evident that the gas sensor response increases when the concentration of the analyte is increased. Furthermore, at ppb levels (100 and 500 ppb), pristine WO_3 was not able to detect H_2S, whereas by the addition of Cu_2O, the detection limit has been improved and is now below 300 ppb.

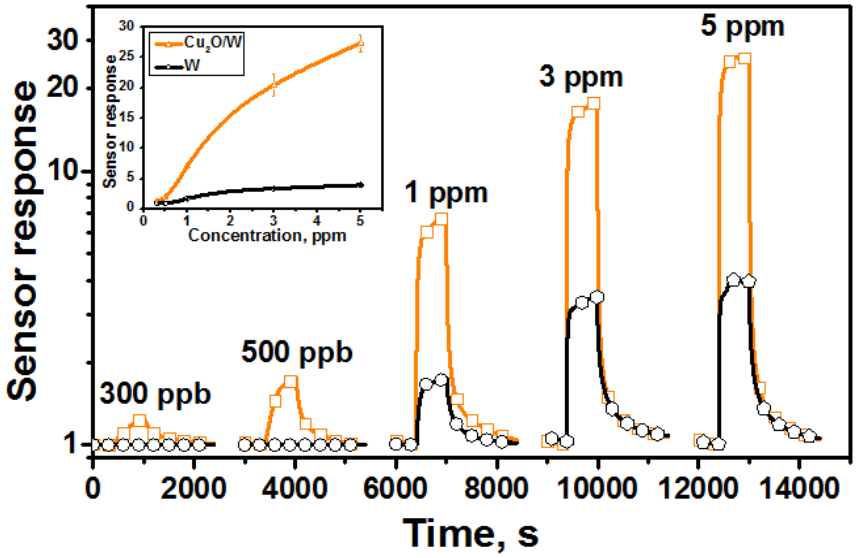

Figure 7. Sensor response to various concentrations of H_2S at 390 °C. The inset shows the curves of the response vs. concentration.

Figure 8 shows an example of the responses recorded from pristine WO_3 and Cu_2O/WO_3 sensors toward 1 ppm of H_2S at 390 °C. Overall, the sensors behave as an *n*-type semiconductor, i.e. decreasing the resistance when exposed to a reducing gas (H_2S). The sensors displayed stable and reproducible responses, and no drift in the response was observed. It is well known that the quality of the semiconductor based gas sensor material affects the stability of the sensor and thus, the high crystallinity of our WO_3 nanoneedles is responsible for the high stability of the sensors.

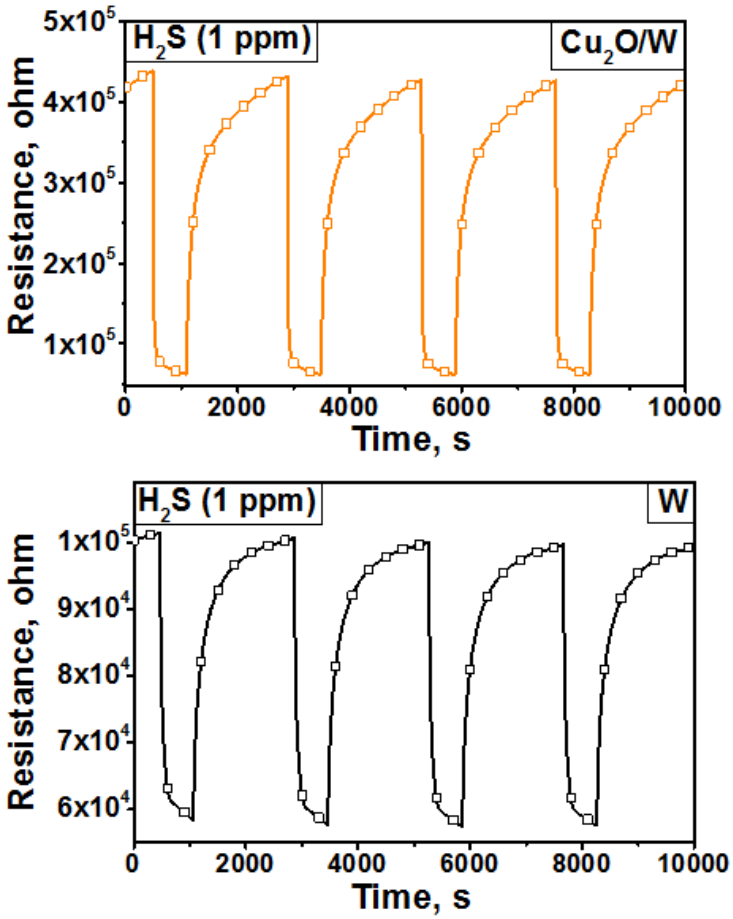

Figure 8. Example of the responses recorded from pristine WO_3 (bottom) and Cu_2O/WO_3 (top) sensors toward 1 ppm of H_2S at 390 °C.

In addition, we can see from the response curves that the decoration with Cu_2O nanoparticles of the WO_3 nanoneedles results in the baseline resistance of the sensor being increased. Cu_2O is a well-known *p*-type semiconductor and WO_3 is an *n*-type one, thus, *p*-*n* junctions are formed at the interfaces of the Cu_2O/WO_3 nanocomposite. The formation of these, leads to the appearance of a space charge layer around each Cu_2O/WO_3 interface, which decreases the free electrons in the conduction band of WO_3 nanoneedles and, therefore, increases the baseline resistance of the sensor.[32] At 5 ppm of H_2S, the response and recovery times were calculated for pristine and decorated WO_3 nanoneedles (Figure 9). The results indicate that Cu_2O decorated samples responded nearly six times faster (i.e., 2 s) than non-functionalized samples (i.e., 11 s). By

comparing this result with the ones reported in the literature for metal/ metal oxide NPs functionalized metal oxide nanowires nanocomposite films, it can be concluded that such a fast response time has not been reported until now. A complete recovery of the baseline resistance was observed within 1100 s after the removal of H_2S, and this for both pristine and decorated samples.

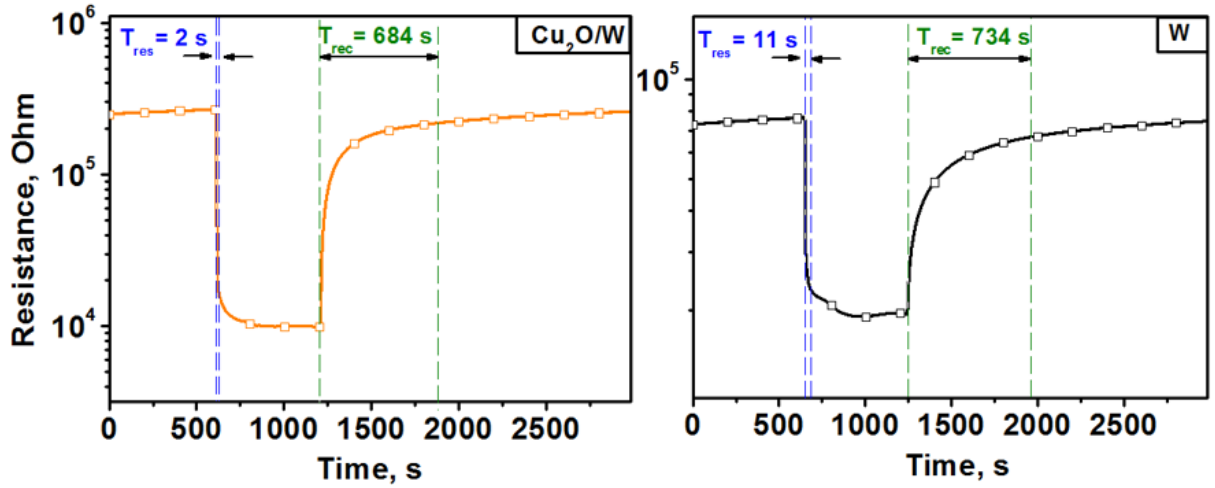

Figure 9. Enlarged responses of functionalized and non-functionalized WO_3 sensors to 5 ppm H_2S at 390 °C. The response time, T_{res}, and recovery time, T_{rec}, correspond to the 90% of change in the electrical resistance of the samples.

The selectivity of the sensors toward H_2S was studied by measuring the response to different interfering gases such as H_2 (500 ppm), CO (50 ppm), NH_3 (50 ppm), C_6H_6 (30 ppm) and NO_2 (40 ppb). All these concentrations are much higher than those one could expect to find in ambient air.[33] As shown in Figure 10, it is clear that Cu_2O decorated WO_3 nanoneedle sensors are more sensitive to low concentration of H_2S (5 ppm) than to the high concentrations of the interfering gases.

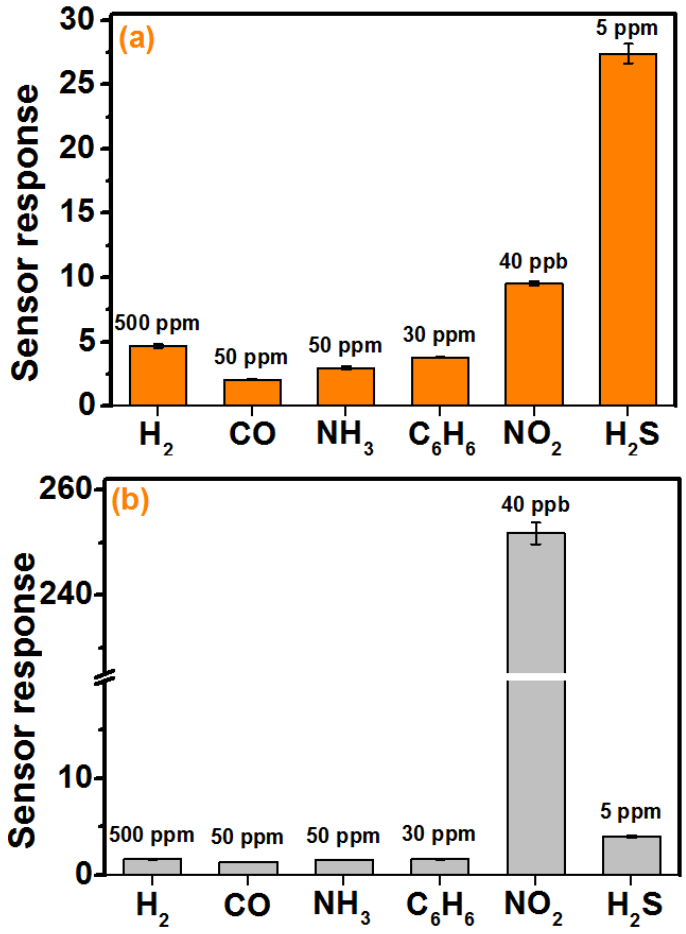

Figure 10. Selectivity diagram of functionalized and non-functionalized WO_3 gas sensors toward different gases at 390 ºC.

The response of the Cu_2O/WO_3 sensor to H_2S is almost 7 times higher than to H_2 and C_6H_6, 13 times higher than to CO, and 9 times higher than to NH_3 vapors. It is worth noting that Cu_2O decorated WO_3 nanoneedles show significant cross-sensitivity to NO_2, as opposed to pure WO_3 nanoneedles, which show an ultra-high sensitivity toward trace concentrations of NO_2 (i.e., more than one hundred times higher than to the other species studied). Therefore, the combination of two sensors, namely, a Cu_2O decorated and a pristine WO_3 nanoneedle sensor in a H_2S detector would enable the suppression of the NO_2 cross-sensitivity.

Gas sensing mechanism

It has been shown that Cu_2O decorated WO_3 nanoneedles exhibit a remarkably improved H_2S response when compared to pristine WO_3 nanoneedles. To explain the sensing mechanism for hydrogen sulfide, the surface adsorption and reaction model illustrated in Figure 11 is suggested. When pristine WO_3 nanoneedles are exposed to air, oxygen molecules can adsorb on their surface and form chemisorbed oxygen species such as O_2^-, O^- or O^{2-}. The nature of oxygen adsorbates depends on the operating temperature (Equation 1-4) and, above 300 ºC, the predominant oxygen ions adsorbed are $O^{2-}_{(lattice)}$.[30] Oxygen adsorbates lead to the formation of an electron depletion layer since they trap electrons from the conduction band of the *n*-type tungsten oxide nanoneedles, which makes the material highly resistive.

When the sensor is exposed to H_2S, the chemisorbed oxygen species (O^{2-}*(lattice)*) can react with the reducing gas molecules giving H_2O (g) and SO_2 (g) following Equation 5,[16,34] while the electrons, originally trapped at oxygen adsorbates will be released, which eventually results in a decrease in the resistance of the nanoneedles mat (Figure 11.a).

$$O_{2(g)} \rightarrow O_{2(ads)} \quad (1)$$

$$O_{2(ads)} + e^- \rightarrow O^-_{2(ads)} \qquad < 100\ °C \quad (2)$$

$$O^-_{2(ads)} + e^- \rightarrow 2O^-_{(ads)} \qquad 100 < T < 300\ °C \quad (3)$$

$$O^-_{(ads)} + e^- \rightarrow O^{2-}_{(lattice)} \qquad > 300\ °C \quad (4)$$

$$H_2S_{(g)} + 3\ O^{2-}_{(lattice)} \rightarrow SO_{2(g)} + H_2O + 6e^- \quad (5)$$

In contrast, Cu_2O/CuO decorated WO_3 nanoneedles show a different mechanism (Figure 11.b and c). Cu_2O/CuO nanoparticles and WO_3 nanoneedles are *p*-type and *n*-type semiconductor oxides, respectively. The contact between these two different materials leads to the formation of numerous *p-n* heterojunctions and electron depletion layers at the interface between WO_3

nanoneedles and Cu_2O/CuO nanoparticles. Upon exposure to H_2S, three simultaneous reactions can take place:

One corresponds to the interaction between the studied gas and the chemisorbed oxygen, which is described above the Equation 5. The two others correspond to the interaction between H_2S molecules and Cu_2O/CuO nanoparticles. According to Equation 6 and 7, Cu_2O and CuO are converted to metallic Cu_2S and CuS respectively, by an oxygen/sulphur replacement mechanism,[35] while the *p-n* heterojunctions are destroyed. Hence, a large number of electrons is released in the WO_3 nanoneedles and a dramatic decrease in the resistance of the nanocomposite mat can be measured.

$$Cu_2O_{(s)} + H_2S_{(g)} \rightarrow Cu_2S_{(s)} + H_2O_{(g)} \quad (6)$$

$$CuO_{(s)} + H_2S_{(g)} \rightarrow CuS_{(s)} + H_2O_{(g)} \quad (7)$$

In the recovery phase, where synthetic air is flushed to clean the sensor surface, the copper oxides are regenerated according to Equation 8 and 9, the *p-n* heterojunctions are restored and the material resistance returns to its original high value.

$$Cu_2S_{(s)} + \frac{1}{2}O_{2(g)} \rightarrow Cu_2O_{(s)} + SO_{2(g)} \quad (8)$$

$$CuS_{(s)} + \frac{3}{2}O_{2(g)} \rightarrow CuO_{(s)} + SO_{2(g)} \quad (9)$$

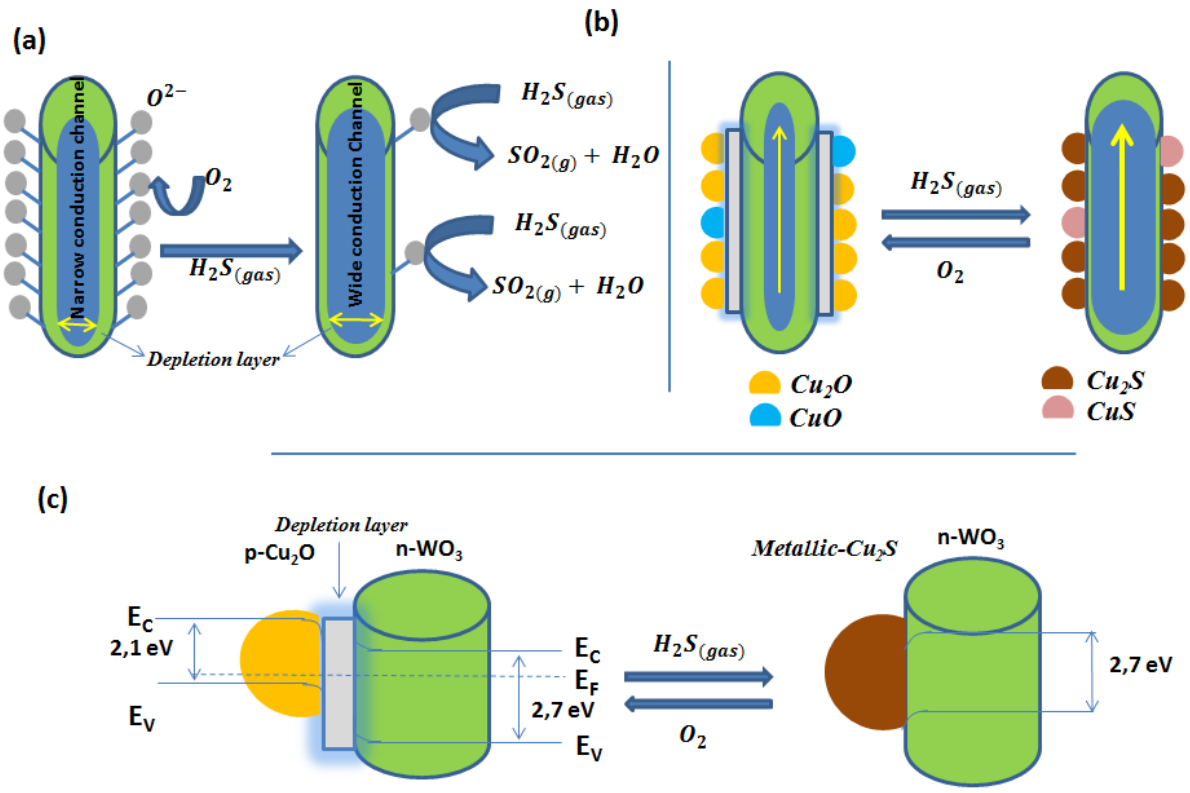

Figure 11. H_2S gas sensing mechanism of (a) pure WO_3 nanoneedles, (b) Cu_2O/CuO functionalized WO_3 nanoneedles, and an example of the *p-n* heterojunction of the Cu_2O nanoparticles/WO_3 nanoneedles before and after H_2S analyte (c).

Humidity cross-sensitivity

The influence of water vapor is a key factor to be taken in consideration for the development of chemoresistive metal oxide gas sensors. Ambient moisture can produce notable changes in the electrical properties of metal oxides and dramatically influences sensitivity.

To study the effect of humidity, the response of the sensors toward 5 ppm of H_2S at an operating temperature of 390 ºC was monitored both under dry and humid (50% R.H. @ 25 ºC) conditions. Figure 12 shows two consecutive cycles of response to H_2S and recovery in air under humid and dry conditions.

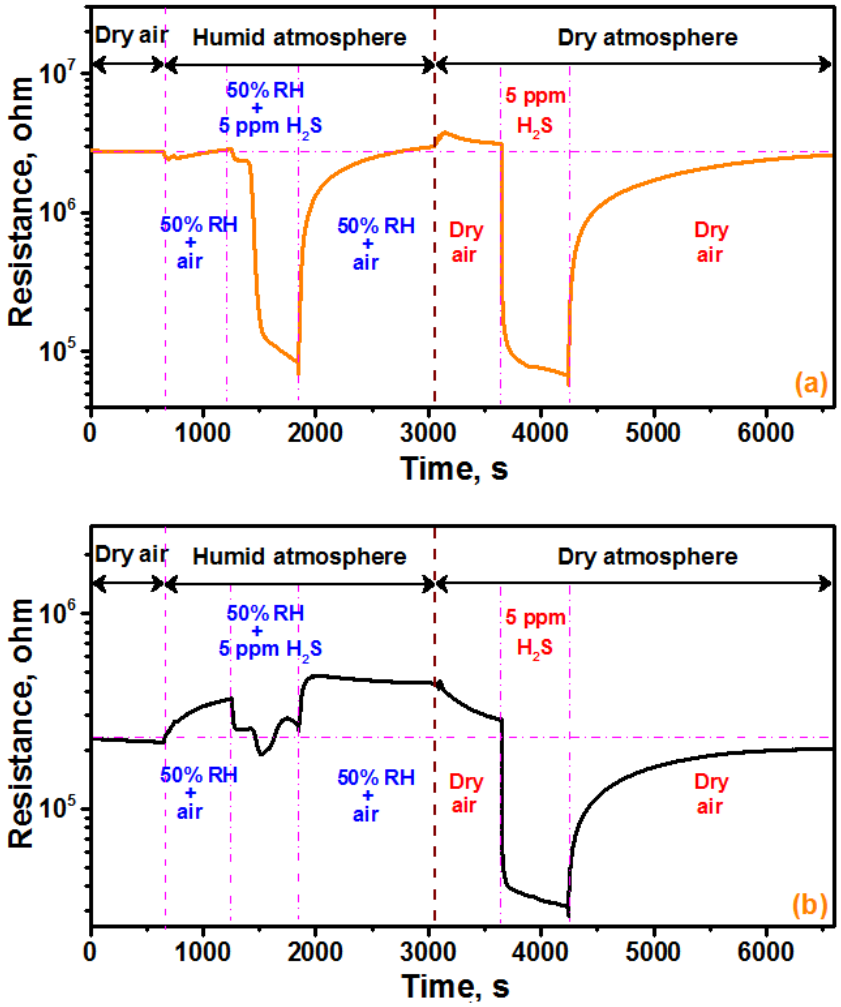

Figure 12. Sensor resistance variation of (a) functionalized and (b) non-functionalized WO3 nanoneedles toward dry and humid (50% R.H. @ 25 ºC) atmospheres in a background of synthetic air and 5 ppm of H2S in synthetic air.

From these results, it can be derived that there is a high influence of ambient moisture on the response of pristine WO_3 nanoneedles. When humid air is introduced in the background, the resistance of the pristine WO_3 sensor is increased by 40% compared to its baseline resistance in dry air. This increase in the resistance under humid conditions has been reported before for SnO_2, ZnO and In_2O_3.[36] Under humid conditions, the response of pristine WO_3 nanoneedles to H_2S is dramatically reduced by 82%, which indicates the occurrence of a competition between

water molecules (formation of hydroxyl groups) and H_2S for active sites. It is well-known that there is a high dependence between the effect of humidity on sensor response and the relative surface distribution of hydroxyl groups and oxygen species.[36] When humidity is removed, the baseline resistance is restored and so is sensor response to H_2S.

For Cu_2O decorated WO_3 nanoneedles, small changes in the baseline resistance (below 5%) and response to H_2S (below 15%) can be observed when the sensor is operated under humid or dry conditions. The fact that the sensor baseline and the response mechanism to H_2S are dominated by the *p*-*n* heterojunctions brought in by the presence of Cu_2O nanoparticles, rather than by surface oxygen species, explains the high immunity of this nanomaterial to dramatic changes in background humidity. A summary of the sensing properties of the Cu_2O/WO_3 nanomaterial and a comparison with those reported by previously published works can be found in the Supporting Information.

Conclusions

Due to its simplicity, relatively low setup and running costs and its scalability, AACVD is an industrially attractive technique. Because it is an atmospheric pressure process the rates of deposition that are typically orders of magnitude higher than those of low pressure processes, which allows for the direct and fast growth of nanomaterials onto a wide spectrum of substrates. WO_3 nanoneedles decorated with Cu_2O nanoparticles were successfully grown onto MEMS gas sensor substrates via a single-step AACVD. The gas sensing results have revealed that the decoration of tungsten oxide nanoneedles with Cu_2O nanoparticles dramatically increases their response to H_2S (i.e., a 700% increase in comparison to that of pristine tungsten oxide nanoneedles). A low detection limit below 300 ppb has been demonstrated. Furthermore, this

hybrid nanomaterial shows the fastest response time ever reported (2 s) and very low moisture cross-sensitivity, which is rarely found in metal oxides. Consequently, these results pave the way for a new generation of nanotechnology-enabled H_2S analyzers with superior performance.

Experimental Section

Functionalized and non-functionalized WO_3 nanoneedles were directly deposited on MEMS micro-hotplates using the AACVD method. Figure 13 depicts four microsensor platforms, each one contains $POCl_3$-doped polysilicon double spiral shape heaters (16 Ω/sq, 0.47 μm thick, and TCR: 6.79×10^{-4}/ºC) and platinum electrodes (0.2 μm thick, electrode gap: 50 μm). To electrically insulate the electrodes on top from the heater, 800 nm thick silicon oxide layers were produced at wafer-level following various microfabrication steps including implantation, photolithography, metallization, lift-off and rear side etching of the substrate to define the membranes. The synthesis of pristine WO_3 nanoneedles was carried out via AACVD of tungsten hexacarbonyl (50 mg, $W(CO)_6$, Sigma-Aldrich, ≥97%) dissolved in a mixture of acetone and methanol (15 mL acetone and 5 mL of methanol , Sigma-Aldrich, ≥99.6%), whereas the Cu_2O functionalized WO_3 nanoneedles were obtained by mixing tungsten hexacarbonyl (50 mg, $W(CO)_6$, Sigma-Aldrich, ≥97%) dissolved in methanol (16 mL of methanol, Sigma-Aldrich, ≥99.6%) with copper (II) acetylacetonate (7 mg, $Cu(acac)_2$, Sigma-Aldrich, 99.9%) dissolved in chloroform (4 mL chloroform, Sigma-Aldrich). The arrays of four membranes were cleaned with acetone and then with ethanol, dried in air and then placed inside the reactor. A micro-mask was placed on the top of the substrate to cover the electrical connections of the heater and electrodes. The solutions were kept in a glass flask and placed in an ultrasonic humidifier. The aerosol of solvents and the mixture of precursors was transported to the heated zone inside the reactor, by using 500 mL/min of nitrogen as a carrier gas. The exhaust from the reactor was vented directly

into the extraction system of a fume cupboard. The deposition time was between 30 to 45 min, until all the precursor had passed through the reactor. After that, all the samples were subjected to annealing at 500 ºC for 3 h under a constant flow (200 sccm) of synthetic air (Praxair, 99.99%). Finally, the microsensors were wire bonded to standard TO8 packages.

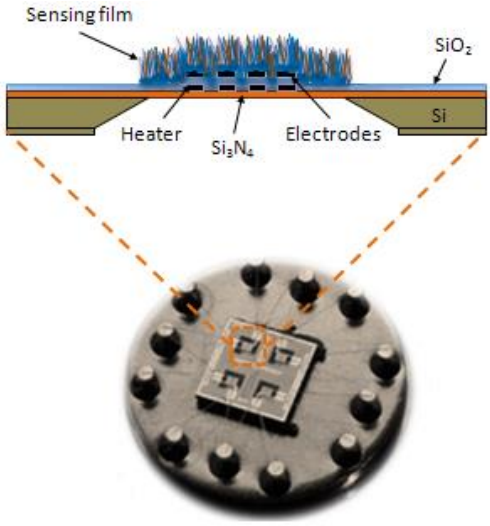

Figure 13. Schematic view of the gas sensor section (a) and photo image of the micromachined sensor mounted on a standard TO-8 package (b). Reproduced with permission.

Surface morphology of the samples was investigated using a scanning electron microscope (SEM-FEI Quanta 600) and transmission electron microscopes (TEM Jeol JEM 1011, operating at 100 kV and Jeol 2100 operated at 200 kV) while the structure of the deposited film was studied by X-ray diffraction (XRD) (Bruker, AXD D8-Discover, using Cu K α radiation operated at 40 kV and 40 mA). The elemental and chemical composition determination were performed by X-ray photoelectron spectroscopy (XPS) (Physical Electronics, VERSAPROBE PHI 5000, using monochromatic Al K α radiation with 0.7 eV energy resolution; a dual-beam charge neutralizer composed of an electron gun (≈ 1 eV) and an argon-ion gun (≤ 10 eV) for charge compensation; all of the binding energies were calibrated to the C 1s peak at 284.5 eV).

To study the electronic structure of a single wire, near-edge x-ray absorption fine-structure spectroscopy (NEXAFS-TXM) was performed with the full-field transmission x-ray microscope installed at the undulator beamline U41-SGM at the electron storage ring BESSY II operated by the Helmholtz-Zentrum Berlin.[37] The spectra were recorded at room temperature in a transmission mode by taking a sequence of images over a range of photon energies covering the investigated absorption edges with a spectral resolution larger than 5000. The used zone plate allowed a spatial resolution of 25 nm. The NEXAFS spectra were normalized since the photon flux varies as a function of photon energy ($h \cdot \upsilon$) and position in the object field (x, y). The normalization was performed by dividing the function I(x, y, $h \cdot \upsilon$) recorded on the sample by the photon flux curve I_0(x+Dx, y+Dy, $h \cdot \upsilon$) recorded in its sample free proximity at position (x+Dx, y+Dy). Both I(x, y, $h \cdot \upsilon$) and I_0 (x, y, $h \cdot \upsilon$) were recorded in the same image stack, since near each studied nanostructure bare regions permit the measurement of I_0.

Gas sensing test of the sensors were carried out in a Teflon/Stainless steel test chamber (2×10^{-2} dm^3), under a continuous gas flow of 200 sccm. The resistance change of the different samples while exposed to different concentrations of the studied gases and vapors was monitored by using an Agilent-34970A multimeter. The desired concentrations of the test gases were obtained employing calibrated gas bottles and PC-driven mass flow controllers (Bronkhost Hitech 7.03.241). Humidity measurements were performed using an Environics, Series 4000, which allowed us to automatically mix up to three individual gases in a balance gas (air, pollutant gas and humidity). The sensors were exposed to the test gas during 10 min, and subsequently the chamber was purged with air during 30 minutes, which enabled recording the recovery of their baseline resistance. After this process, the sensors were ready for a new measurement. The sensor response (R) was defined as $R = R_a/R_g$ for reducing gases and $R = R_g/R_a$ for oxidizing

gases, where R_a and R_g are the sensor resistance at stationary state in air and after 10 min of exposure to analytes, respectively. Moreover, the response time is defined as the time needed by the sensor to reach a fixed percentage (e.g. 110%) of its steady-state resistance value when it is exposed to a reducing gas (H_2S), whereas, the recovery time is outlined as the time need by the sensor to return to a fixed percentage (e.g. 90 %) of the saturation value of its resistance when it is subjected to a clean air.

ASSOCIATED CONTENT

Supporting Information Available. A summary of the sensing properties of the Cu_2O/WO_3 nanomaterial. Comparison with previously published works. This material is available free of charge via the Internet at http://pubs.acs.org.

ACKNOWLEDGMENT

This work has been supported in part by the Spanish Ministry of Science and Innovation via grant no. TEC2012-32420 and also by the Catalan Institution for Research and Advanced Studies via the ICREA Academia Award (EL). We thank HZB for the allocation of synchrotron radiation beamtime. The research leading to these results has received funding from the European Community's Seventh Framework Programme (FP7/2007-2013) under grant agreement no. 226716 (ELISA) and no. 312284 (CALIPSO). CB is a Research Associate of the National Funds for Scientific Research (FRS-FNRS, Belgium). SV is supported by the 'South Moravian Programme - SoMoPro' via grants 4SGA8678.

REFERENCES

1. a) Vallejos, S.; Stoycheva, T.; Annanouch, F. E.; Llobet, E.; Umek, P.; Figueras, E.; Cané, C.; Gracia, I.; Blackman, C. Microsensors based on Pt–nanoparticle functionalised

tungsten oxide nanoneedles for monitoring hydrogen sulfide. *RSC Adv.*, **2014**, *4*, 1489–1495. b) Ghosh, S.; RoyChaudhuri, C.; Bhattacharya, R.; Saha, H.; Mukherjee, N. Palladium–Silver-Activated ZnO Surface: Highly Selective Methane Sensor at Reasonably Low Operating Temperature. *ACS Appl. Mater. Interfaces.* **2014**, *6*, pp. 3879–3887. c) Zhang, S.; Zhang, P.; Wang, Y.; Ma, Y.; Zhong, J.; Sun, X. Facile Fabrication of a Well-Ordered Porous Cu-Doped SnO_2 Thin Film for H_2S Sensing. *ACS Appl. Mater. Interfaces.* **2014**, *6*, pp. 14975–14980.

2. a) He, L.; Jia, Y.; Meng, F.; Li, M.; Liu, J. Development of sensors based on CuO-doped SnO2 hollow spheres for ppb level H_2S gas sensing. *J. Mater. Sci.,* **2009**, *44*, 4326–4333. b) North Carolina Department of Environment and Natural Resources, Summary of Rule Amending the Hydrogen Sulfide Acceptable Ambient Level, http://daq.state.nc.us/toxics/studies/H2S/, accessed: March, **2006**. c) Wagh, M. S.; Patil, L. A.; Seth, T.; Amalnerkar, D. P. Surface cupricated SnO_2–ZnO thick films as a H_2S gas sensor. *Mater. Chem. Phys*, **2004**, *84*, 228–233. d) Meng, F.; Di, X.; Dong, H.; Zhang, Y.; Zhu, C.; Li, C.; Chen, Y. Ppb H_2S gas sensing characteristics of Cu_2O/CuO sub-microspheres at low-temperature. *Sens. Actuators, B* **2013**, *182*, 197–204.

3. Qi, G.; Zhang, L.; Yuan, Z. Improved H_2S gas sensing properties of ZnO nanorods decorated by a several nm ZnS thin layer. *Phys.Chem.Chem.Phys.,* **2014**, *16*, 13434–13439.

4. a) Ghimbeu, C. M.; Lumbreras, M.; Siadat, M.; Landschoot, R. C.; Schoonman, J. Electrostatic sprayed SnO_2 and Cu-doped SnO_2 films for H_2S detection. *Sens. Actuators, B* **2008**, *133*, 694–698. b) Kaur, M.; Jain, N.; Sharma, K.; Bhattacharya, S.; Roy, M.; Tyagi, A. K.; Gupta, S. K.; Yakhmi, J. V. Room-temperature H_2S gas sensing at ppb level by single crystal In_2O_3 whiskers. *Sens. Actuators, B* **2008**, *133*, 456–461.

5. Samokhvalov, A.; Tatarchuk, B. J. Characterization of Active Sites, Determination of Mechanisms of H_2S, COS and CS_2 Sorption and Regeneration of ZnO Low-Temperature Sorbents: Past, Current and Perspectives. *Phys. Chem. Chem. Phys.,* **2011**, *13*, 3197–3209.

6. Stoycheva, T.; Annanouch, F. E.; Gràcia, I.; Llobet, E.; Blackman, C.; Correig, X.; Vallejos, S. Micromachined gas sensors based on tungsten oxide nanoneedles directly integrated via aerosol assisted CVD. *Sens. Actuators, B* **2014**, *198*, 210–218.

7. a) Giebelhaus, I.; Varechkina, E.; Fischer, T.; Rumyantseva, M.; Ivanov, V.; Gaskov, A.; Morante, J. R.; Arbiol, J.; Tyrra, W.; Mathur, S. One-dimensional CuO–SnO_2 p–n heterojunctions for enhanced detection of H_2S. *J. Mater. Chem. A,* **2013**, *1*, 11261–11268. b) Pandey, S. K.; Kim, K.H.; Tang, K. T. A review of sensor-based methods for monitoring hydrogen sulfide. *Trends Anal. Chem.,* **2012**, *32*, 87–99. c) Kim, S. S.; Na, H. G.; Choi, S. W.; Kwak, D. S.; Kim, H. W.; Novel growth of CuO-functionalized, branched SnO_2 nanowires and their application to H_2S sensors. *J. Phys. D: Appl. Phys.,* **2012**, *45*, 205301. d) Xiaoyuan, J.; Huijuan, L.; Xiaoming, Z. Catalytic activity of CuO-loaded TiO_2/γ-Al_2O_3 for NO Reduction by CO. *J. Mater. Sci.,* **2008**, *43*, 6505–6512. e) Woo, H. S.; Kwak, C. H.; Kim, I. D.; Lee, J. H. Selective, sensitive, and reversible H_2S sensors using Mo-doped ZnO nanowire network sensors. *Mater. Chem. A*, **2014**, *2*, 6412– 6418.

8. a) Gurlo, A. Nanosensors: towards morphological control of gas sensing activity. SnO_2, In_2O_3, ZnO and WO_3 case studies. *Nanoscale,* **2011**, *3*, 154–165. b) Shen, G.; Chen, D.; Chen, P.; Zhou, C. Vapor−Solid Growth of One-Dimensional Layer-Structured Gallium Sulfide Nanostructures. *ACS Nano,* **2009**, *3*, 1115–1120.

9. Vallejos, S.; Umek, P.; Stoycheva, T.; Annanouch, F.; Llobet, E.; Correig, X.; De Marco, P.; Bittencourt, C.; Blackman, C. Single-step deposition of Au- and Pt-nanoparticle-functionalized tungsten oxide nanoneedles synthesized via aerosol-assisted CVD, and used for fabrication of selective gas microsensor arrays. *Adv. Funct. Mater.*, **2013**, *23,* 1313–1322.

10. Riaz, A.; Jung, K.; Chang, W.; Shin, K.; Lee. J. Carbon-, Binder-, and Precious Metal-Free Cathodes for Non-Aqueous Lithium–Oxygen Batteries: Nanoflake-Decorated Nanoneedle Oxide Arrays. *ACS Appl. Mater. Interfaces.* **2014**, *6*, pp. 17815–17822.

11. Kolmakov, A.; Klenov, D. O.; Lilach, Y.; Stemmer, S.; Moskovits, M. Enhanced gas sensing by individual SnO_2 nanowires and nanobelts functionalized with Pd catalyst particles. *Nano Lett.,* **2005**, *5*, 4667–4673.

12. Van, P. T. H.; Thanh, N. H.; Quang, V. V.; Duy, N. V.; Hoa, N. D.; Hieu, N. V. Scalable Fabrication of High-Performance NO_2 Gas Sensors Based on Tungsten Oxide Nanowires by On-Chip Growth and RuO_2-Functionalization. *ACS Appl. Mater. Interfaces.* **2014**, *6*, pp. 12022–12030.

13. a) Annanouch, F. E.; Stoycheva, T,; Vallejos, S.; Blackman, C.; Correig, X.; Llobet, E. AA-CVD growth and ethanol sensing properties of pure and metal decorated WO_3 nanoneedles. *IJNT*, **2013**, *10,* 455–469. b) Vallejos, S.; Stoycheva, T.; Umek, P.; Navio, C.; Snyders, R.; Bittencourt, C.; Llobet, E.; Blackman, C. ; Moniz, S.; Correig, X. Au nanoparticle-functionalised WO_3 nanoneedles and their application in high sensitivity gas sensor devices *Chem. Commun.*, **2011**, *47*, 565–567.

14. Zanolli, Z.; Leghrib, R.; Felten, A.; Pireaux, J.; Llobet, E.; Charlier, J. Gas Sensing with Au-Decorated Carbon Nanotubes. *ACS Nano,* **2011**, *5*, 4592–4599.

15. a) Palgrave, R. G.. Parkin, I. P. Aerosol Assisted Chemical Vapor Deposition Using Nanoparticle Precursors: A Route to Nanocomposite. *J. Am. Chem. Soc.*, **2006**, *128*, 1587–1597. b) Hill, M. S.; Johnson, A. L.; Manning, T. D.; Molloy, K. C; Wickham, B. J. Single-source AACVD of composite cobalt-silicon oxide thin films. *Inorg. Chim. Acta.*, **2014**, *422,* 47–56.

16. Shao, F.; Hoffmann, M. W. G.; Prades, J. D.; Zamania, R.; Arbiol, J.; Morante, J. R.; Varechkina, E.; Rumyantseva, M.; Gaskov, A.; Giebelhaus, I.; Fischer, T.; Mathur, S.; Hernández-Ramírez, F. Heterostructured p-CuO (nanoparticle)/n-SnO_2 (nanowire) devices for selective H_2S detection. *Sens. Actuators, B* **2013**, *181*, 130–135.

17. Sun, G. J.; Choi, S. W.; Katoch, A.; Wu, P.; Kim, S. S. Bi-functional mechanism of H_2S detection using CuO–SnO_2 nanowires. *Mater. Chem. C,* **2013**, *1*, 5454– 5462.

18. Wang, C.; Chu, X.; Wu, M. Detection of H_2S down to ppb levels at room temperature using sensors based on ZnO nanorods. *Sens. Actuators, B* **2006**, *113*, 320–323.

19. Annanouch, F. E.; Vallejos, S.; Stoycheva, T.; Blackman, C.; Llobet, E. Aerosol assisted chemical vapour deposition of gas-sensitive nanomaterials. *Thin Solid Films,* **2013**, *548*, 703–709.

20. Annanouch, F. E.; Camara, M.; Ramírez, J. L.; Briand, D.; Llobet, E. Gas sensing properties of metal-decorated tungsten oxide nanowires directly grown onto flexible polymeric hotplates. *Proc. Eng.,* **2014**, *87,* 700–703.

21. Vallejos, S.; Umek, P.; Blackman, C. Aerosol Assisted Chemical Vapour Deposition Control Parameters for Selective Deposition of Tungsten Oxide Nanostructures. *J. Nanosci. Nanotechnol.*, **2011**, *11*, 8214–8220.

22. Navío, C.; Vallejos, S.; Stoycheva, T.; Llobet, E.; Correig, X.; Snyders, R.; Blackman, C.; Umek, P.; Ke, X.; Tendeloo, G. V.; Bittencourt, C. Gold clusters on WO_3 nanoneedles grown via AACVD: XPS and TEM studies. *Mater. Chem. Phys.*, **2012**, *134*, 809–813.

23. Xie, F. Y.; Gong, L.; Liu, X.; Tao, Y. T.; Zhang, W. H.; Chen, S. H.; Meng, H.; Chen, J. XPS studies on surface reduction of tungsten oxide nanowire film by Ar^+ bombardment. *J. Electron Spectrosc. Relat. Phenom.,* **2012**, *185*, 112–118.

24. Ottaviano, L.. Bussolotti, F.. Lozzi, L.; Passacantando, M.; La Rosa, S.; Santucci, S. Core level and valence band investigation of WO_3 thin films with synchrotron radiation. *Thin Solids Films,* **2003**, *436,* 9–16.

25. Bussolotti, F.; Lozzi, L.; Passacantando, M.; La Rosa, S.; Santucci, S.; Ottaviano, L. Surface electronic properties of polycrystalline WO_3 thin films: a study by core level and valence band photoemission *Surf. Sci.* **2003**, *538*, 113–123.

26. Leftheriotis, G.; Papaefthimiou, S.; Yiannoulis, P.; Siokou, A. Effect of the tungsten oxidation states in the thermal coloration and bleaching of amorphous WO_3 films. *Thin Solid Films*, **2001**, *384,* 298–306.

27. Wong, H. Y.; Ong, C. W.; Kwok, R. W.; Wong, K. W.; Wong, S. P.; Cheung, W. Y. Effects of ion beam bombardment on electrochromic tungsten oxide films studied by X-ray photoelectron spectroscopy and Rutherford back-scattering. *Thin Solid Films*, **2000**, *376,* 131–139.

28. Gurevich, A. B.; Bent, B. E.; Teplyakov, A. V.; Chen, J. G. A NEXAFS investigation of the formation and decomposition of CuO and Cu_2O thin films on Cu(100). *Surf. Sci.*, **1999**, *442*, L971– L976.

29. Grioni, M.; Goedkoop, J. B.; Schoorl, R.; De Groot, F. M. F.; Fuggle, J. C.; Schäfers, F.; Koch, E. E.; Rossi, G.; Esteva, J. M.; Karnatak, R. C. Studies of copper valence states with Cu L3 x-ray-absorption spectroscopy. *Phys. Rev. B*, **1989**, *39*, 1541–1545.

30. Bai, S.; Zhang, K.; Luo, R.; Li, D.; Chena, A.; Liu, C. C. Low-temperature hydrothermal synthesis of WO_3 nanorods and their sensing properties for NO_2. *J. Mater. Chem.*, **2012**, *22*, 12643–12650.

31. Song, P.; Han, D.; Zhang, H.; Li, J.; Yang, Z.; Wang, Q. Hydrothermal synthesis of porous In_2O_3 nanospheres with superior ethanol sensing properties. *Sens. Actuators, B* **2014**, *196*, 434–439.

32. Tong, P. V.; Hoa, N. D.; Quang, V. V.; Duy, N. V.; Hieu, N. V. Diameter controlled synthesis of tungsten oxide nanorod bundles for highly sensitive NO_2 gas sensors. *Sens. Actuators, B* **2013**, *183*, 372–380.

33. EU, D., 50/EC of the European Parliament and of the Council of 21 May 2008 on ambient air quality and cleaner air for Europe. *Official Journal of the European Union,* **2008**, L152.

34. a) Wang, L.; Kang, Y.; Wang, Y.; Zhu, B.; Zhang, S.; Huang, W.; Wang, S. CuO nanoparticle decorated ZnO nanorod sensor for low-temperature H_2S detection. *Mater. Sci. Eng. C*, **2012** *32*, 2079–2085. b) Hien, V. X.; You, J.; Jo, K.; Kim, S.; Lee, J.; Kim, J.; Heo, Y. H_2S-

sensing properties of Cu_2O submicron-sized rods and trees synthesized by radio-frequency magnetron sputtering. *Sens. Actuators, B* **2014**, *202*, 330–338.

35. Galtayries, A.; Bonnelle, J. P. XPS and ISS studies on the interaction of H_2S with polycrystalline Cu, Cu_2O and CuO surfaces. *Surf. Interface Anal.*, **1995**, *23*, 171–179.

36. a) Bai, Z.; Xie, C.; Hu, M.; Zhang, S.; Zeng, D. Effect of humidity on the gas sensing property of the tetrapod-shaped ZnO nanopowder sensor. *Mater. Sci. Eng. B*, **2008**, *149,* 12–17. b) Merdrignac-Conanec, O.; Bernicot, Y.; Guyader, J. Humidity effect on baseline conductance and H_2S sensitivity of cadmium germanium oxynitride thick film gas sensors. *Sens. Actuators, B* **2000**, *63*, 86–90. c) Choi, K.; Kim, H.; Kang, Y. C.; Lee, J. Ultraselective and ultrasensitive detection of H_2S in highly humid atmosphere using CuO-loaded SnO_2 hollow spheres for real-time diagnosis of halitosis. *Sens. Actuators, B* **2014**, *194*, 371–376. d) Barsan, N.; Weimar, U. Understanding the fundamental principles of metal oxide based gas sensors; the example of CO sensing with SnO_2 sensors in the presence of humidity. *J. Phys. Condens. Matter,* **2003**, *15*, 813–839.

37. Guttmann, P.; Bittencourt, C.; Rehbein, S.; Umek, P.; Ke, X.; Tendeloo, G. V.; Ewels, C. P.; Schneider, G. Nanoscale spectroscopy with polarized X-rays by NEXAFS-TXM. *Nat. Photonics,* **2011**, *6,* 25–29.